

This article may be downloaded for personal use only. Any other use requires prior permission of the author and AIP Publishing. This article appeared in W. C. Young, A. B. Hassam, C. A. Romero-Talamás, R. F. Ellis, C. Teodorescu; Diamagnetism of rotating plasma. Phys. Plasmas 18 (11): 112505. <https://doi.org/10.1063/1.3660536> and may be found at <https://pubs.aip.org/aip/pop/article-abstract/18/11/112505/378187/Diamagnetism-of-rotating-plasma?redirectedFrom=fulltext>.

Access to this work was provided by the University of Maryland, Baltimore County (UMBC) ScholarWorks@UMBC digital repository on the Maryland Shared Open Access (MD-SOAR) platform.

Please provide feedback

Please support the ScholarWorks@UMBC repository by emailing scholarworks-group@umbc.edu and telling us what having access to this work means to you and why it's important to you. Thank you.

RESEARCH ARTICLE | NOVEMBER 16 2011

Diamagnetism of rotating plasma

W. C. Young; A. B. Hassam; C. A. Romero-Talamás; R. F. Ellis; C. Teodorescu



Phys. Plasmas 18, 112505 (2011)

<https://doi.org/10.1063/1.3660536>



CrossMark



APL Machine Learning

Latest Articles Online!

Read Now



Diamagnetism of rotating plasma

W. C. Young,^{a)} A. B. Hassam, C. A. Romero-Talamás, R. F. Ellis, and C. Teodorescu
IREAP, University of Maryland, College Park, Maryland 20742, USA

(Received 29 July 2011; accepted 17 October 2011; published online 16 November 2011)

Diamagnetism and magnetic measurements of a supersonically rotating plasma in a shaped magnetic field demonstrate confinement of plasma pressure along the magnetic field resulting from centrifugal force. The Grad-Shafranov equation of ideal magnetohydrodynamic force balance, including supersonic rotation, is solved to confirm that the predicted angular velocity is in agreement with spectroscopic measurements of the Doppler shifts. © 2011 American Institute of Physics. [doi:10.1063/1.3660536]

Most magnetic geometries for confining plasma for fusion are “closed” in the sense that the Larmor orbits of the charged particles stay spatially localized, tightly bound to magnetic field lines that close on themselves. Configurations with “open” field lines intercepting chamber walls, however, may have advantages such as requiring simpler coil configurations. Magnetic mirror geometry is one such example, where the charged particles are confined by bouncing away from the mirror throats due to the adiabatic conservation of the gyro-averaged magnetic moment, though collisions detract these orbits. If, however, a radial electric field is imposed on mirror geometry, the $\mathbf{E} \times \mathbf{B}$ drift of the particles results in a radial, centrifugal force, with a component along the field line that is inward toward the machine’s midplane, leading to confinement.^{1–6} The centrifugal force axially confines particles even under collisions as all orbits at given energy are centrifugally trapped.

In this article, we present a clear demonstration of localization of high pressure plasma parallel to the magnetic field by directly linking parallel pressure gradients to axial variations in plasma diamagnetism as measured by an array of diamagnetic and radial magnetic flux loops. Plasma diamagnetism is usually associated with diamagnetic currents from plasma pressure gradients; here, we also confirm the theoretically predicted diamagnetic currents arising from the bulk MHD kinetic energy of plasma rotation. An earlier paper⁷ showed density localization along the field lines via interferometric measurements and correlated the density localization with flux measurements. The present paper constitutes an independent confirmation of density localization and a direct comparison between theory and experiment. In addition to the application to mirror geometry, the centrifugal effect can apply similarly to other axisymmetric confinement geometries with rotation^{8,9} and astrophysical systems such as Jupiter’s magnetosphere^{10,11} and accretion disks.¹²

The experiments were performed on the Maryland centrifugal experiment (MCX).⁶ MCX has a magnetic mirror geometry with an axial, metallic core (see Figure 1). The core is biased negatively, initially 6–16 kV, with respect to the grounded vacuum vessel to ionize the fill gas and to provide a radial electric field. The plasma is limited axially by

insulating disks at the mirror throats, and radially, the plasma is confined to flux lines not intersecting the conducting core or vacuum vessel. For a typical mirror ratio 7 configuration, this limits the plasma to radii between 8 cm and 26 cm at the midplane.

Wound azimuthally around the exterior of the vacuum vessel are nine flux loops (diamagnetic loops or DMLs). Six of these loops provide a detailed axial profile of changes in the enclosed axial magnetic flux along one half of the machine, while the other three test the symmetry across the midplane. The measurements from the DMLs can be expressed as flux, or average B_z (averaged over the cross section of the loop). There is also an array of 16 magnetic pick-up coils, each 8.5 cm in diameter, evenly spaced azimuthally on the outside of the vacuum vessel, and oriented to measure B_r . This azimuthal array can be moved to any z position between 10 and 60 cm. Additional pick-up loops measure B_r in the z range of 70–90 cm. B_r measurements are averaged over the azimuthal arrays at a given z location to remove an azimuthal locked mode perturbation. The density is measured at the midplane and at a second location 91 cm from the

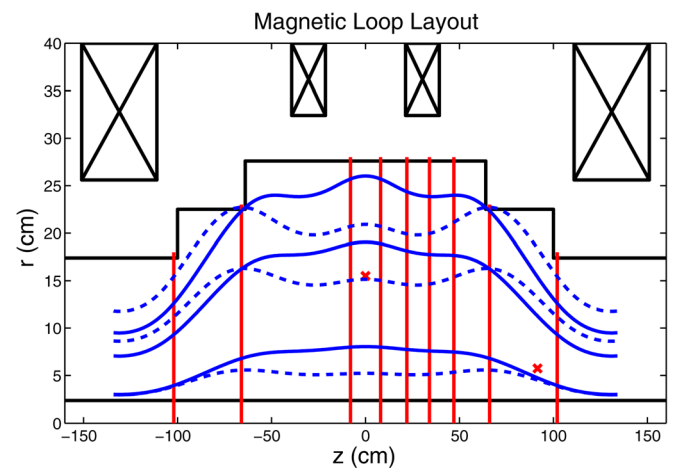


FIG. 1. (Color online) MCX experiment configuration, with vacuum magnetic field lines in blue (solid for mirror ratio 7, dotted for mirror ratio 3), DMLs as vertical red lines, interferometer chords as red crosses, and the vacuum vessel, core and magnet coils in black. The machine is cylindrically symmetric, with the centerline along the bottom of the figure. The radial dimension is exaggerated here, as the largest radius of the vacuum vessel is 28 cm and length between mirror throats is 2.6 m.

^{a)}Electronic mail: wcyoung@umd.edu.

midplane, each by an IR (3.36 μm) interferometer. Lastly, 10 chord spectrometry data provide estimates of impurity rotation velocity radial profiles, via Doppler shift, at either the midplane or 80 cm from the midplane.

A typical discharge consists of prefilling the chamber with 5 mTorr of hydrogen and applying bias voltage of 10 kV to yield a break down. After break down, the voltage across the plasma settles to 3–4 kV. After 5 ms, a short is applied between the core and ground, crowbarring the plasma. Within this time, the density reaches a maximum 0.5 ms after breakdown, while the time-integrated DML signal peaks after about 1.5–2.0 ms. The peaks of different magnetic field measurements differ by at most 0.2 ms; any measurements discussed hereinafter refer to an average over the period 3.5–4.5 ms after breakdown, at the end of a shot just before crowbarring when the L/R response time of the vacuum vessel (about 0.5 ms) has had time to settle. Similarly, spectroscopy observations are from an exposure over the same 1 ms window.

In cylindrical coordinates (r, θ, z) with azimuthal symmetry, the MCX magnetic field can be written as $\mathbf{B} = \nabla\theta \times \nabla\psi$, $\psi = \psi(r, z)$ being the flux function. The plasma experiences an $\mathbf{E} \times \mathbf{B}$ rotation given, in steady state, by $\Omega(\psi)\nabla\psi = \mathbf{u} \times \mathbf{B}$, where Ω is the angular velocity. This rotation yields an azimuthal flow that is rigid-rotor in the MHD limit on each flux line, viz, $\mathbf{u} = \hat{\theta}r\Omega(\psi)$. Under the above conditions, the \mathbf{B} component of the MHD force balance condition, $\rho\mathbf{u} \cdot \nabla\mathbf{u} = -\nabla p + \mathbf{j} \times \mathbf{B}$, is

$$\mathbf{B} \cdot \nabla p = \rho \mathbf{B} \cdot \nabla(r\Omega)^2/2 \quad (1)$$

and the $\nabla\psi$ component yields the Grad-Shafranov equation generalized to include azimuthal flows

$$\nabla \cdot \left(\frac{1}{r^2} \nabla\psi \right) = -\frac{\partial p}{\partial\psi} + \frac{\rho\Omega^2}{2} \frac{\partial r^2}{\partial\psi}. \quad (2)$$

Here $\partial p/\partial\psi \equiv (\partial p/\partial\psi)_\chi$, where χ is the coordinate orthogonal to ψ and θ surfaces.

If we assume the temperature is constant on each field line, $T = T_0(\psi)$, the parallel force balance equation is integrable and yields

$$\rho(\psi, r) = \rho_0(\psi) \exp[r^2\Omega^2/2c_s^2], \quad (3)$$

where $c_s^2 \equiv T_0/M$. For this paper, we assume $T_e \ll T_i$, as expected for the MCX. For MCX, the vacuum magnetic field is the largest energy density. Thus, we expand the Grad-Shafranov equation about the vacuum field ψ_0 . Letting $\psi = \psi_0 + \tilde{\psi}$, we obtain the linearized Grad-Shafranov equation

$$\nabla \cdot \left(\frac{1}{r^2} \nabla\tilde{\psi} \right) = -\mu_0 \left[\frac{\partial(n_0 T_0)}{\partial\psi_0} + m_p n_0 T_0^2 \frac{\partial}{\partial\psi_0} \left(\frac{\Omega^2}{2T_0} \right) \right] \times \exp\left(\frac{m_p r^2 \Omega^2}{2T_0} \right). \quad (4)$$

The two terms on the right hand side of Eq. (4) represent, in order, the diamagnetism arising from the plasma pressure and that arising from the bulk rotational kinetic energy.

Equation (4) has two key features. The first is the right hand side can be shown to scale quadratically with M_A , the rotational Alfvén Mach number. Such a trend has been previously observed, even across diverse changes in plasma parameters.¹³ The second is the exponential dependence on the rotational velocity, which can be expressed dimensionlessly as an exponential dependence on M_s , the rotational sonic Mach number, and radius. The exponential factor arises from the centrifugal localization of pressure, such that a model lacking this factor would lack centrifugal confinement. The impact of this factor can be checked against the data as a test for centrifugal confinement.

The solution for $\tilde{\psi}$ is governed by the vacuum field and the three profiles over ψ_0 : T_0 , Ω , and n_0 . $\tilde{\psi}$ can be solved with a standard numeric elliptical partial differential equation solver, using an assumed parabolic profiles for $T_0(\psi)$, $n_0(\psi)$, and $\Omega(\psi)$ (going to zero at the inner and outer last good flux surface). The magnitude of n_0 is constrained by the interferometer, where the average over the profile along the interferometer's chord must match the average density measured by the interferometer.

Ω can be estimated by spectrometer Doppler measurements of CIII ion impurities. At the speeds observed (~ 100 km/s), drift orbit theory would predict the rotation speeds of CIII and H ions should be similar on account of the $\mathbf{E} \times \mathbf{B}$ drift independence of ion mass and that curvature and gradient drifts are much smaller.¹⁴ The first order correction to the $\mathbf{E} \times \mathbf{B}$ drift, however, is of the order of ρ_L/a , proportional to the carbon Larmor radius and inversely proportional to a radial scale a . This correction is dependent on mass and charge. When considering rotation velocities of isolated ions accelerated only by the radial electric field, in which case $\rho_L \propto m/q$, CIII ions could have rotational velocities up to 20% slower than H ions, for rotational velocities of about 100 km/s. However, H-CIII collisional energy equilibration rates compared to MCX confinement times are large, $\tau_{conf}^E \nu_{C-H}^E \sim 10 - 30$; thus, the temperatures of carbon and hydrogen ions are expected to be significantly equilibrated. With the Larmor radius from thermal velocities giving $\rho_L \propto \sqrt{mT}/q$, the equilibrated temperature limits the difference between the ions' rotation velocities and results in a velocity difference smaller than the 20% upper bound.

Spectroscopy measurements can also estimate ion temperatures from Doppler broadening, although actual ion temperature may be lower due to broadening from turbulence. Doppler broadening measurements are limited by spectrometer resolution and instrument broadening, resulting in temperature broadening measurements more sensitive to noise than measurements of shifts from bulk velocity. Additionally, recent improvements to vacuum quality have reduced the presence of impurities and the strength of their lines, reducing the availability of reliable temperature measurements.

Thus, to account for lack of temperature measurement, and the discrepancies in the velocity measurements, we take the approach in our analysis that the peak temperature and rotation are to be deduced through a best fit of the model to magnetic measurements. We then compare the Doppler measurements to the best fit.

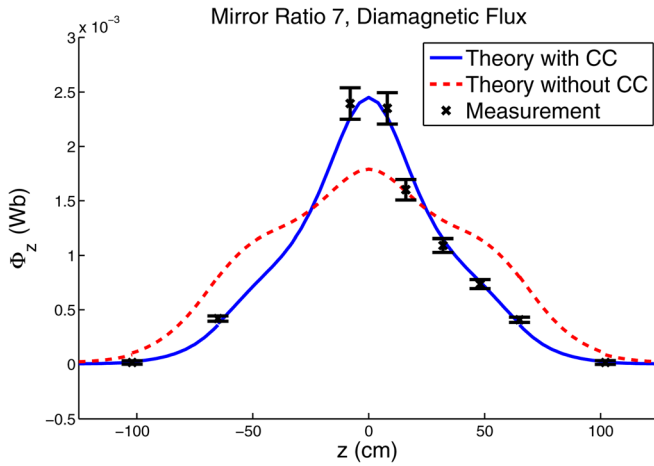


FIG. 2. (Color online) Flux measurements from DMLs, expressed as flux across the whole loop, for mirror ratio 7 shots with predicted values shown in blue for peak rotation velocity of 130 km/s and temperature of 14 eV. The red, dotted curve shows the theory without the centrifugal confinement factor. Peak flux corresponds to an average B_z of 100 G across the flux loop.

For mirror ratios higher than 5, profiles of B_z flux form a steep peak near the midplane as in Figure 2. For the shots shown, the mirror ratio was 7 and the midplane field was 2 kG. The peak flux corresponds to an average B_z of 105 ± 10 G, giving a $\Delta B/B \sim 5\%$, justifying the modeling as a perturbation. Fitting the peak rotation velocity and temperature found 130 ± 20 km/s and 14 ± 4 eV, respectively, yielding the curve plotted in blue. Spectroscopic measurements found a peak impurity rotation velocity of 106 ± 11 km/s. In addition, Figure 3 shows the B_r profile for the same shots and fitted values as used in the B_z flux plot. Doppler broadening has previously given an upper bound on ion temperatures of 30 ± 10 eV.⁷

For mirror ratios below 5, the geometry of the coils leads to the appearance of two off-midplane field minima at

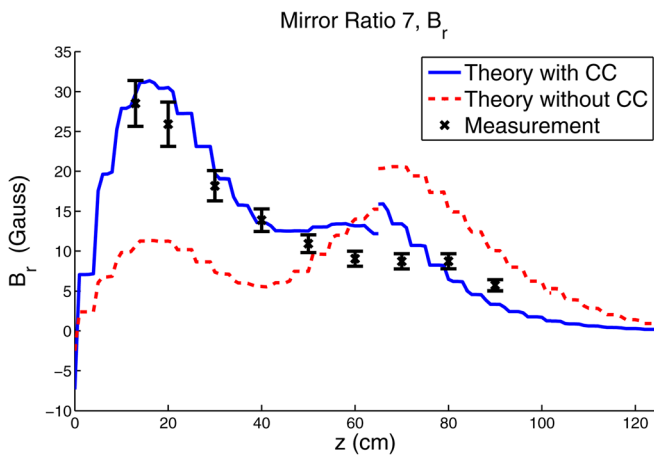


FIG. 3. (Color online) B_r measurements from pick-up coils, for a mirror ratio 7 shots. Theory is shown in blue for peak rotation of 130 km/s and temperature of 14 eV, while shown in red/dotted without the centrifugal confinement factor. Measurements for $z < 65$ cm are taken at a $r = 28$ cm, and those for $z > 65$ cm are taken at $r = 22$ cm, hence there is a discontinuity in the theory due to the change in radius. The jagged nature of the curve is from differentiating a linearly interpolated solution.

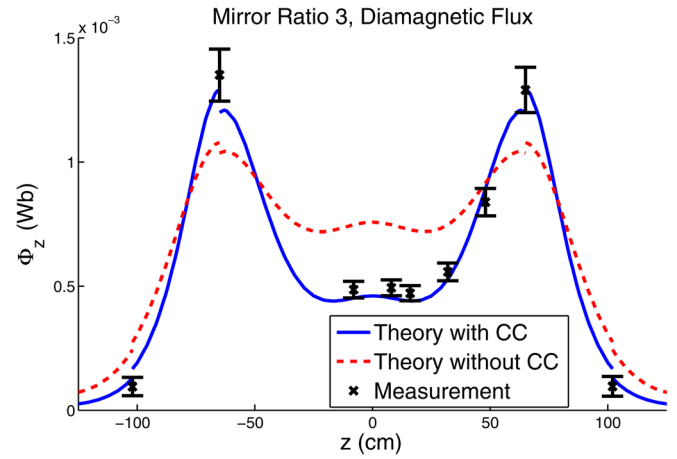


FIG. 4. (Color online) Diamagnetic flux measured by DMLs for mirror ratio 3 shots, with theory is shown in solid blue and without centrifugal confinement factor in dotted red.

$z = \pm 65$ cm (see dotted field lines in Figure 1). At mirror ratio 3 with the same midplane field of 2 kG, these side minima are about 88% of the midplane field, with the last good flux surface extending radially outward 2-3 cm more at off-midplane than at midplane. This gives a contrasting case to the mirror ratio 7 profiles, as seen in Figures 4 and 5. Here, the fitting results in a peak temperature of 2.7 ± 0.7 eV and a peak rotation velocity of 56 ± 6 km/s at $z = 75$, as compared to the measured impurity rotation velocity of 70 ± 20 km/s at the same z .

To demonstrate the significance of the exponential factor in the density and solution for $\tilde{\psi}$, the mirror ratio 7 and 3 cases are refitted with this factor artificially set to 1. Although this factor has peak values of up to 2000 previously, the magnitude of the density is constrained by the interferometer measurement, leading to only a change in profile shape from turning off this factor. Refitting the model as such is plotted in red, dotted curves in all of the profile plots. There is a qualitative difference between magnetic measurements and the shapes of the profiles given by this modification. With non-centrifugal diamagnetism, $\Delta B_z/B_z \propto \beta$ giving $\Delta B_z \propto 1/B_z$.

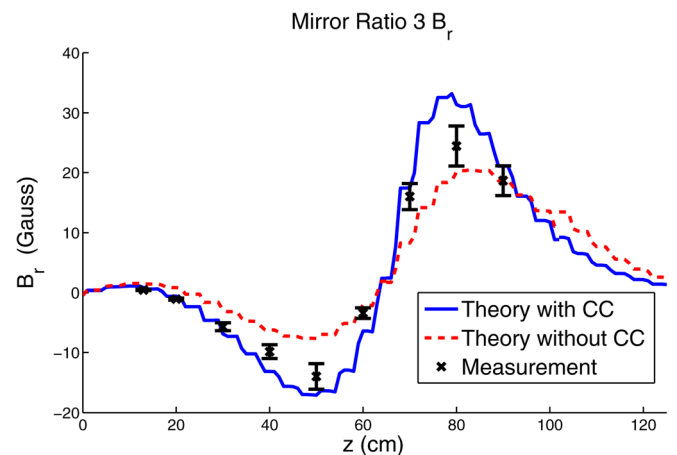


FIG. 5. (Color online) B_r measured for mirror ratio 3 shots, with theory is shown in solid blue and without centrifugal confinement factor in dotted red.

Hence the plasma field will always reflect the shape of vacuum field and cannot form a B_z profile as peaked as the measured plasma field. Similarly, the peaks of B_r profile cannot match the proportions seen in the measurements.

The magnetic measurements have two dominant sources of errors: uncertainty in position/angle of the loops and shot-to-shot variation. For the DMLs, these two errors are comparable in size. The smaller B_r loops have more uncertainty in their angle relative to the radial direction and are more sensitive to such uncertainty due to the strong B_z component. As a result, the error from position is a factor of 2–3 larger than variation between shots.

The MHD Grad-Shafranov theory in this paper was developed assuming isothermal temperature along each magnetic field line. This is not an unreasonable assumption as numerical simulations suggest that temperature profiles in the z direction form a plateau,¹⁵ only dropping off close to the insulators at the end of the machine. In addition, the Braginskii parallel electron thermal conductivity has a strong temperature dependence that also results in plateau-like axial temperature profiles. Relaxing this assumption using a more general solver of Eq. (2) could improve agreement between theory and measurement, especially with B_r measurements and the mirror ratio 3 cases, which are more sensitive to variation along z .

In conclusion, the magnetic measurements demonstrate plasma diamagnetism from bulk plasma rotation as predicted

by ideal MHD theory and strongly confirm the presence of the predicted phenomenon of centrifugal confinement.

¹B. Lehnert, *Nucl. Fusion* **11**, 485 (1971).

²V. N. Bocharov, N. A. Zavadskii, A. V. Kiselev, S. G. Konstantinov, A. M. Kudryavtsev, O. K. Myskin, V. M. Panasyuk, and F. Tsel'nik, *Pis'ma Zh. Eksp. Teor. Fiz.* **41**, 494 (1985).

³J. G. Bannenberg and G. J. Brakenhoff, *Plasma Phys.* **13**, 587 (1971).

⁴G. F. Abdrashitov, A. V. Beloborodov, V. I. Volosov, V. V. Kubarev, Y. S. Popov, and Y. N. Yudin, *Nucl. Fusion* **31**, 1275 (1991).

⁵K. Boyer, J. E. Hammel, C. L. Longmire, D. Nagle, F. Ribe, and W. B. Riesenfeld, in *Proceedings of the 2nd International Conference on Peaceful Uses of Atomic Energy*, United Geneva, 1–13 September 1958.

⁶R. F. Ellis, A. Case, R. Elton, J. Ghosh, H. Griem, A. Hassam, R. Lunsford, S. Messer, and C. Teodorescu, *Phys. Plasmas* **12**, 055704 (2005).

⁷C. Teodorescu, W. C. Young, G. W. S. Swan, R. F. Ellis, A. B. Hassam, and C. A. Romero-Talamas, *Phys. Rev. Lett.* **105**, 085003 (2010).

⁸J. E. Menard, R. E. Bell, E. D. Fredrickson, D. A. Gates, S. M. Kaye, B. P. LeBlanc, R. Maingi, S. S. Medley, W. Park, S. A. Sabbagh, A. Sontag, D. Stutman, K. Tritz, and W. Zhu, *Nucl. Fusion* **45**, 539 (2005).

⁹L. Guazzotto, J. P. Freidberg, and J. Kesner, *Phys. Plasmas* **14**, 062501 (2007).

¹⁰G. Caudal, *J. Geophys. Res.* **91**, 4201, doi:10.1029/JA091iA04p04201 (1986).

¹¹G. Zimbardo, *J. Geophys. Res.* **94**, 8707, doi:10.1029/JA094iA07p08707 (1989).

¹²J. Fukue and R. Okada, *Publ. Astron. Soc. Jpn.* **42**, 249 (1990).

¹³C. Teodorescu, R. Clary, R. F. Ellis, A. B. Hassam, R. Lunsford, I. Uzun-Kaymak, and W. C. Young, *Phys. Plasmas* **15**, 042504 (2008).

¹⁴J. Ghosh, R. C. Elton, H. R. Griem, A. Case, A. W. DeSilva, R. F. Ellis, A. Hassam, R. Lunsford, and C. Teodorescu, *Phys. Plasmas* **13**, 022503 (2006).

¹⁵Y.-M. Huang and A. B. Hassam, *Phys. Rev. Lett.* **87**, 235002 (2001).